

RESEARCH ARTICLE

10.1002/2015GC005858

Effect of maghemization on the magnetic properties of nonstoichiometric pseudo-single-domain magnetite particles

Trevor P. Almeida<sup>1</sup>, Adrian R. Muxworthy<sup>1</sup>, Takeshi Kasama<sup>2</sup>, Wyn Williams<sup>3</sup>, Christian Damsgaard<sup>2,4</sup>, Cathrine Frandsen<sup>4</sup>, Timothy J. Pennycook<sup>5,6,7</sup>, and Rafal E. Dunin-Borkowski<sup>8</sup>

Special Section:

Magnetism From Atomic to Planetary Scales: Physical Principles and Interdisciplinary Applications in Geo- and Planetary Sciences

Key Points:

- Maghemization of Fe<sub>3</sub>O<sub>4</sub> grains is confirmed through XRD, Mossbauer, and EELS
- Maghemization of Fe<sub>3</sub>O<sub>4</sub> grains occurs through formation of a core-shell structure
- Magnetic behavior is considered due to core-shell exchange coupling

Correspondence to:

T. P. Almeida, t.almeida@imperial.ac.uk

Citation:

Almeida, T. P., A. R. Muxworthy, T. Kasama, W. Williams, C. Damsgaard, C. Frandsen, T. J. Pennycook, and R. E. Dunin-Borkowski (2015), Effect of maghemization on the magnetic properties of nonstoichiometric pseudo-single-domain magnetite particles, *Geochem. Geophys. Geosyst.*, 16, 2969–2979, doi:10.1002/2015GC005858.

Received 9 APR 2015

Accepted 30 JUL 2015

Accepted article online 6 AUG 2015

Published online 12 SEP 2015

<sup>1</sup>Department of Earth Science and Engineering, Imperial College London, London, UK, <sup>2</sup>Center for Electron Nanoscopy, Technical University of Denmark, Kongens Lyngby, Denmark, <sup>3</sup>School of GeoSciences, University of Edinburgh, Edinburgh, UK, <sup>4</sup>Department of Physics, CINP, Technical University of Denmark, Kongens Lyngby, Denmark, <sup>5</sup>SuperSTEM Laboratory, Daresbury, UK, <sup>6</sup>Department of Materials, University of Oxford, Oxford, UK, <sup>7</sup>Now at Physics of Nanostructured Materials Group, Faculty of Physics, University of Vienna, Vienna, Austria, <sup>8</sup>Ernst Ruska-Centre for Microscopy and Spectroscopy with Electrons and Peter Grünberg Institute, Forschungszentrum Jülich, Jülich, Germany

**Abstract** The effect of maghemization on the magnetic properties of magnetite (Fe<sub>3</sub>O<sub>4</sub>) grains in the pseudo-single-domain (PSD) size range is investigated as a function of annealing temperature. X-ray diffraction and transmission electron microscopy confirm the precursor grains as Fe<sub>3</sub>O<sub>4</sub> ranging from ~150 to ~250 nm in diameter, whilst Mössbauer spectrometry suggests the grains are initially near-stoichiometric. The Fe<sub>3</sub>O<sub>4</sub> grains are heated to increasing reaction temperatures of 120–220°C to investigate their oxidation to maghemite (γ-Fe<sub>2</sub>O<sub>3</sub>). High-angle annular dark field imaging and localized electron-energy loss spectroscopy reveal slightly oxidized Fe<sub>3</sub>O<sub>4</sub> grains, heated to 140°C, exhibit higher oxygen content at the surface. Off-axis electron holography allows for construction of magnetic induction maps of individual Fe<sub>3</sub>O<sub>4</sub> and γ-Fe<sub>2</sub>O<sub>3</sub> grains, revealing their PSD (vortex) nature, which is supported by magnetic hysteresis measurements, including first-order reversal curve analysis. The coercivity of the grains is shown to increase with reaction temperature up to 180°C, but subsequently decreases after heating above 200°C; this magnetic behavior is attributed to the growth of a γ-Fe<sub>2</sub>O<sub>3</sub> shell with magnetic properties distinct from the Fe<sub>3</sub>O<sub>4</sub> core. It is suggested there is exchange coupling between these separate components that results in a vortex state with reduced vorticity. Once fully oxidized to γ-Fe<sub>2</sub>O<sub>3</sub>, the domain states revert back to vortices with slightly reduced coercivity. It is argued that due to a core/shell coupling mechanism during maghemization, the directional magnetic information will still be correct; however, the intensity information will not be retained.

1. Introduction

During formation, magnetic minerals record the direction and intensity of the Earth’s magnetic field. Paleomagnetists use this information to investigate, for example, past tectonic plate motion and geodynamo evolution. However, subsequent to formation, the constituent magnetic minerals are commonly exposed to a range of weathering conditions and environments. One of the most common weathering processes is maghemization, which is the oxidation of (titano)magnetite at ambient temperatures, i.e., the slow oxidation of (titano)magnetite to (titano)maghemite [van Velzen and Zijdeveld, 1995]. Maghemization is known to be very common in mid-ocean ridge basalts >2 Ma [Bleil and Petersen, 1983; Matzka et al., 2003], and understanding this general process is important as maghemization that is known to alter the original remanent magnetization [Krása et al., 2005].

Of the constituent magnetic minerals, particles in the single domain (SD) grain size range (<100 nm) are regarded as ideal paleomagnetic recorders because of their strong remanence and high magnetic stability, with potential relaxation times greater than that of the age of the Universe [Dunlop and Özdemir, 2001]. However, magnetic signals from rocks are often dominated by small grains with nonuniform magnetization that exhibit magnetic recording fidelities similar to those of SD grains (termed pseudo-SD (PSD)).

In this paper, the progressive oxidation/maghemization of PSD magnetite (Fe<sub>3</sub>O<sub>4</sub>) to maghemite (γ-Fe<sub>2</sub>O<sub>3</sub>) is investigated. Oxidation of PSD Fe<sub>3</sub>O<sub>4</sub> grains is a critical process of alteration of remanent magnetic signals and must be fully understood to allow for reliable interpretation of paleomagnetic data. The oxidation process starts at the Fe<sub>3</sub>O<sub>4</sub> surface, where Fe<sup>2+</sup> is either partially removed from the crystal or it reacts with

© 2015. The Authors.

This is an open access article under the terms of the Creative Commons Attribution License, which permits use, distribution and reproduction in any medium, provided the original work is properly cited.

oxygen to form a new crystal layer [O'Reilly, 1984]. Further oxidation is driven by the oxidation gradient where  $\text{Fe}^{2+}$  diffuses from the interior of the grain to the surface, leaving vacancies in the interior. Hence, depending on the degree of oxidation, the  $\text{Fe}_3\text{O}_4$  grains can be altered to structures ranging from a thin oxidized  $\gamma\text{-Fe}_2\text{O}_3$  surface layer, a hetero-structured core-shell  $\text{Fe}_3\text{O}_4/\gamma\text{-Fe}_2\text{O}_3$  grain or a fully oxidized  $\gamma\text{-Fe}_2\text{O}_3$  grain.

Recent work using the transmission electron microscopy (TEM) technique of off-axis electron holography combined with environmental TEM visually showed a change in both strength and direction of remanent magnetization within PSD  $\text{Fe}_3\text{O}_4$  particles, as a consequence of in situ oxidation within the TEM [Almeida *et al.*, 2014]. This study is very important as it directly confirmed that oxidation can modify the original magnetic signal within individual  $\text{Fe}_3\text{O}_4$  particles in the size range dominant in rocks. However, due to the reduced  $\text{O}_2$  atmosphere pressures (<10 mbar) permitted for these in situ experiments, it was necessary to use elevated temperatures (800°C) to induce oxidation and hence is not directly representative of nature. Owing to the localized aspect of this study, it was limited to analysis of only a few individual PSD  $\text{Fe}_3\text{O}_4$  particles and it is therefore perhaps incorrect to generalize this magnetic behavior to the larger numbers of grains within rocks. In this context, the ex situ oxidation of a bulk powder comprised entirely of PSD  $\text{Fe}_3\text{O}_4$  grains, at comparatively lower temperatures, is reported. The chemical and structural transformation associated with low-temperature oxidation of the PSD  $\text{Fe}_3\text{O}_4$  particles is related directly to their corresponding magnetic properties. This work is similar in objective to several previous studies [e.g., Liu *et al.*, 2004; Ge *et al.*, 2014]; however, unlike the previous studies, advanced TEM methods and Mössbauer spectroscopy, in addition to magnetic hysteresis and X-ray diffractometry (XRD), are applied.

## 2. Experimental

Synthetic  $\text{Fe}_3\text{O}_4$  particles (diameter ranging from ~150 to ~250 nm) were purchased from Nanostructured and Amorphous Materials, USA. For heating experiments, discreet samples of 30 mg native  $\text{Fe}_3\text{O}_4$  powder (Sample S1) were mixed with 20 ml ethanol in a beaker and dispersed using an ultrasonic bath. Dispersions were poured into a glass petri dish and then inserted into a temperature-controlled furnace at reaction temperatures of 120, 140, 160, 180, 200, and 220°C under ambient atmosphere (denoted as Samples S120–S220). To promote a uniform powder distribution, dispersions were heated until the ethanol had evaporated (~5 to 10 min), leaving a thin layer of powder, and subsequently heated for a further 2 h. After heating, the petri dish was removed and the dry reaction products were allowed to cool at room temperature.

The synthesized reaction products were deposited onto single crystal silicon substrates for crystallographic identification using XRD (PANalytical X'Pert PRO Diffractometer). For the purpose of TEM, the particles were dispersed in acetone using an ultrasonic bath before deposition onto lacey carbon/copper mesh support grids (Agar Scientific Ltd., UK). Conventional diffraction contrast imaging was performed using an FEI Titan TEM operated at 300 kV (Center for Electron Nanoscopy (CEN), Technical University of Denmark) and selected area electron diffraction (SAED) patterns allowed for phase identification. Electron-energy loss spectroscopy (EELS) analysis was performed at an energy resolution of ~0.3 eV, achieved through excitation of the monochromator, to provide information on sample oxidation state. High-angle annular dark field (HAADF) high-resolution scanning TEM (STEM) analysis was performed using a Nion UltraSTEM 100 at 100 kV (SuperSTEM, STFC Daresbury Laboratories, Daresbury, UK). EELS analysis was performed to measure the oxygen/Fe ratio and was quantified using Digital Micrograph software. The background signal was subtracted and, using the signal quantification parameters determined by the software, the relative area densities in the EEL spectra allowed the relative atomic ratios to be calculated. For the purpose of off-axis electron holography [Dunin-Borkowski *et al.*, 1998], an FEI Titan with a  $\text{C}_5$  probe corrector on the condenser lens, equipped with a Lorentz lens and biprism, was used at 300 kV (CEN). Off-axis electron holograms were recorded in Lorentz mode with the objective lens switched off and the specimen in magnetic-field-free conditions at room temperature. Mean inner potential contributions to the recorded phase shift were removed by using in situ magnetization reversal [Kasama *et al.*, 2011].

The magnetic measurements were conducted at the Natural Magnetism Group Laboratory at the Imperial College London and Technical University of Denmark. High-temperature thermomagnetic curves were measured using a Princeton Measurements vibrating sample magnetometer (VSM) fitted with a furnace

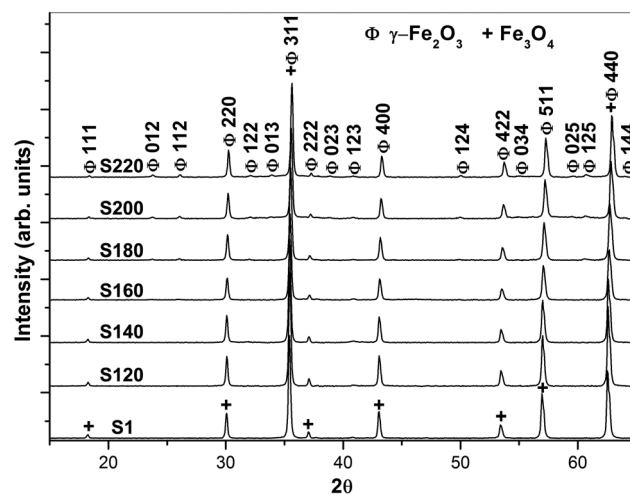


**Figure 1.** Room-temperature XRD patterns of Samples S1–S220 showing the effect of increasing temperature on the oxidation of  $\text{Fe}_3\text{O}_4$  to  $\gamma\text{-Fe}_2\text{O}_3$  (indexed, JCPDS 8-7119).

development of small peaks characteristic to  $\gamma\text{-Fe}_2\text{O}_3$  (JCPDS 8-7119), can be seen with increasing reaction temperature in Samples S160–S220. The findings are in agreement with those of *Ge et al.* [2014] who made similar heating experiments for grains that were  $\sim 80$  to 240 nm in diameter. In addition, the  $2\theta$  values were used to determine the interplanar lattice spacing ( $d$ ) for the {220}, {311}, {400}, {511}, and {440} sets of lattice planes. The lattice parameter ( $a$ ) was calculated from each set of ( $hkl$ ) using the equation for the cubic crystal unit cell [Cullity and Stock, 2001], and the average was determined. The change in lattice parameter  $a$  as a function of reaction temperature is summarized in Table 1.

### 3.2. Transmission Electron Microscopy

Figure 2 provides information on the size, morphology, and crystallographic phase of the initial  $\text{Fe}_3\text{O}_4$  precursor (Sample S1), along with the  $\gamma\text{-Fe}_2\text{O}_3$  sample (S220), produced by heating to 220°C (Sample S220). The bright-field (BF) images of Sample S1 (Figure 2a) displays generally isotropic  $\text{Fe}_3\text{O}_4$  grains ( $\sim 150$  to  $\sim 250$  nm in diameter), as confirmed by SAED (Figure 2a, inset). EELS analysis of the O  $1s$  K edge, in the region 520–580 eV (Figure 2c), is indicative of  $\text{Fe}_3\text{O}_4$  and composed of a prepeak (labeled a); a broad edge at higher energy (labeled b); along with higher-energy-loss structures, lying at about 548 eV (labeled c); and 563–565 eV (labeled d). Prepeak (a) results from the hybridization of Fe  $3d$  and O  $2p$  and usually splits into  $t_{2g}$  and  $e_g$  states by the ligand field. Peak (b) is composed of density of states from oxygen  $p$  character hybridized with metal  $4s$  and  $4p$  states [Colliex et al., 1991]. The higher-energy-loss maxima in the fine structures (labeled c and d) are induced during the final state of the emitted electron, described as superposition, on the core-excited site, of an outgoing wave and of the multiple backscattered waves on the successive shells of neighboring oxygen ions [Colliex et al., 1991]. EELS analysis of the Fe  $2p$   $L_{2,3}$  edge, in the region 704–726 eV (Figure 2d), confirmed the assignment of  $\text{Fe}_3\text{O}_4$ . The  $L_2$  edge for this sample shows the typical shape of a mixed-valence compound, i.e., three visible features of differing intensities (Figure 2d, black arrows), whilst the almost shapeless  $L_3$  edge is attributed to the combined spectral contributions of

**Table 1.** Lattice Parameter of the Unit Cell Determined From the XRD Patterns

Sample	Lattice Parameter $a$ (Å)
S1	8.381
S120	8.373
S140	8.373
S160	8.365
S180	8.355
S200	8.342
S220	8.332

and heating was performed in flowing He. First-order reversal curve (FORC) diagrams and  $^{57}\text{Fe}$  Mössbauer spectra were acquired from the reaction products at room temperature. The Mössbauer spectra are calibrated relative to  $\alpha\text{-Fe}$  at room temperature.

## 3. Results

### 3.1. X-Ray Diffraction Analysis

The XRD patterns of Figure 1 illustrate the effect of increasing temperature on the crystallography of the reaction products. The peaks in the XRD pattern of Samples S1 are in good agreement with the presence of  $\text{Fe}_3\text{O}_4$  (Joint Committee on Powder Diffraction standards (JCPDS) 75-449). Samples S120 and S140 exhibit XRD patterns similar to S1, whilst devel-

different iron sites (i.e.,  $\text{Fe}^{2+}$  at octahedral B-sites and  $\text{Fe}^{3+}$  at both tetrahedral A and octahedral B-sites), consistent with the more delocalized structure of  $\text{Fe}_3\text{O}_4$ , as compared with other mixed iron oxides [Crocobette et al., 1995; Fujii et al., 1999].

Figure 2b displays the  $\gamma\text{-Fe}_2\text{O}_3$  grains formed after heating at 220°C for 2 h (Sample S220), as confirmed by SAED

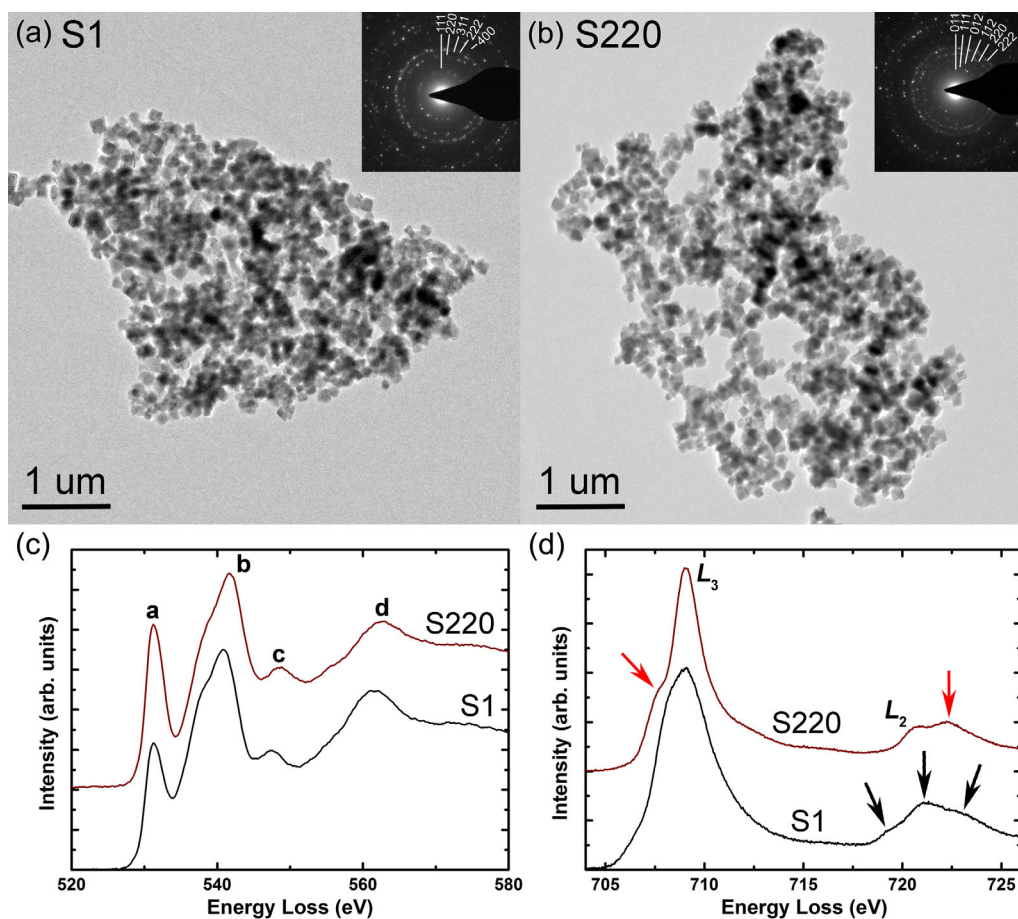


**Figure 2.** Room-temperature BF TEM images of precursor  $\text{Fe}_3\text{O}_4$  particles ( $\sim 150$  to  $\sim 250$  nm in diameter) (a) before (Sample S1); and (b) after heating to  $220^\circ\text{C}$  under an ambient air atmosphere (Sample S220), with associated SAED patterns inset, indexed to (a)  $\text{Fe}_3\text{O}_4$  (JCPDS 75–449) and (b)  $\gamma\text{-Fe}_2\text{O}_3$  (JCPDS 8–7119). Associated EEL spectra of the (c) O  $K$  and (d) Fe  $L_{23}$  edges, which were acquired in diffraction mode with signal emitted from all the  $\text{Fe}_3\text{O}_4$  and  $\gamma\text{-Fe}_2\text{O}_3$  particles in the field of view shown in the TEM images of Figures 2a and 2b.

(Figure 2b, inset). The alteration and development of fine features in the EEL spectra of Sample S220 are indicative of a change in the Fe oxidation state toward  $\gamma\text{-Fe}_2\text{O}_3$  or  $\alpha\text{-Fe}_2\text{O}_3$  [Chen *et al.*, 2004; Gloter *et al.*, 2003; van Aken and Lauterbach, 2003]. An increase in the relative intensity of prepeak (a) in the O  $1s$   $K$  edge with respect to the absorption maximum (b) (Figure 2c, Sample S220) is suggestive of oxidation to  $\gamma\text{-Fe}_2\text{O}_3$ . Similarly, it is recognized that development of a small prepeak in the  $L_3$  edge and post-peak in the  $L_2$  edge of the Fe  $2p$   $L$  edge (Figure 2d, red arrows) are indicative of oxidation, with complete oxidation to  $\gamma\text{-Fe}_2\text{O}_3$  being associated with a  $\sim 1.3$  eV splitting in the  $L_3$  edge [Chen *et al.*, 2009].

The HAADF images of Figure 3 provide a closer examination of an individual  $\text{Fe}_3\text{O}_4$  grain that was heated at  $140^\circ\text{C}$  (Sample S140). Figure 3a shows the grain to be rectangular in this projection, with approximate dimensions of  $\sim 130$  nm long and  $\sim 110$  nm wide. Higher magnification of the boxed region in Figure 3a is displayed in Figure 3b and highlights the characteristic lattice fringes of the  $\{111\}$  set of planes (inset). EEL spectra were acquired from the center, near-edge, and surface regions labeled A, B, and C, respectively, and the associated atomic weight composition (at %) was quantitatively determined from each cumulative EEL spectrum (summarized in Table 2). The data are suggestive of a slightly higher O content present at the surface of the nominally magnetite grain than at its near-edge and center.

Off-axis electron holography allowed for the imaging of the in-plane magnetization of Samples S1 and S220 and is presented in Figures 4 and 5. Figure 4a displays a BF TEM image of an individual native  $\text{Fe}_3\text{O}_4$  grain ( $\sim 180$  nm in diameter) in Sample S1, where the corresponding magnetic induction map (Figure 4b) shows a magnetic vortex and stray magnetic field, revealing its PSD (vortex) nature. Similarly, the BF TEM image of

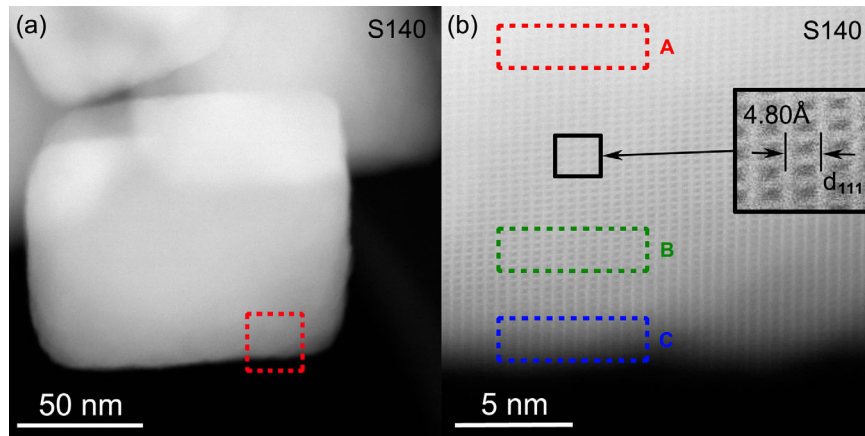


**Figure 3.** HAADF images of Fe<sub>3</sub>O<sub>4</sub> particles heated to 140°C (Sample S140). (a) An individual rectangular Fe<sub>3</sub>O<sub>4</sub> grain, 130 nm long and ~110 nm wide. (b) Magnification of the boxed region in Figure 3a, displaying characteristic lattice fringes of the {111} set of planes. EEL spectra were acquired from boxed regions labeled A, B, and C. Zone axis is <110>.

Figure 5a displays an individual  $\gamma$ -Fe<sub>2</sub>O<sub>3</sub> grain (~200 nm in diameter) in Sample S220, where the corresponding magnetic induction map (Figure 5b) again reveals its PSD (vortex) nature.

### 3.3. Magnetic Properties

The Mössbauer spectra of Figure 6, acquired at room temperature, depict the transition from nonstoichiometric Fe<sub>3</sub>O<sub>4</sub> to  $\gamma$ -Fe<sub>2</sub>O<sub>3</sub> as a function of increasing reaction temperature. Mössbauer parameters were determined by fitting two sextets, St<sub>1</sub> (red) and St<sub>2</sub> (blue), with area ratios of the lines constrained to 3:2:1:1:2:3 for both sextets, using a Lorentzian fitting program called mfit (Table 3). The oxidation state from magnetite to maghemite of the samples was estimated as the magnetite content (wt %) in a magnetite-maghemite mixture, by considering the weighted average isomer shift  $\delta_{aver}$  of the two sextets (Table 3) and using the linear relationship determined in *Da Costa et al.* [2014]:

$$\delta_{aver} \text{ (mm/s)} = 0.335 + 0.00215 * \text{magnetite (wt \%)}$$

The uncertainty of this model is estimated to about 5 wt % magnetite, given that  $\delta_{aver}$  is determined with an error of 0.01 mm/s. The two sextets in the spectrum of S1 exhibit hyperfine parameters which at first may appear similar to pure Fe<sub>3</sub>O<sub>4</sub>, but the weighted average isomer shift of 0.46 mm/s (cf.  $\delta_{aver}$  = 0.55 mm/s for pure magnetite) and the relative spectral area of the two sextets of 0.93 (cf. St<sub>1</sub>/St<sub>2</sub> = 1.9 for pure magnetite) [*Da Costa et al.*, 2014] suggest nonstoichiometric magnetite. Using the model of *Da Costa et al.* [2014], a magnetite content of 59% for Sample S1 is obtained. The spectra of Samples S120–S200 demonstrate further reduction in magnetite content and correspondingly oxidation to maghemite with increasing reaction temperature, as shown in Figure 7a and summarized in Table 3. Samples S200 and S220 display a typical spectrum of  $\gamma$ -Fe<sub>2</sub>O<sub>3</sub>, composed of two sextets with very similar hyperfine parameters [*Da Costa et al.*, 1995]. In addition, the oxidation parameter *z* was determined by comparing the F<sub>B</sub>/F<sub>A</sub> ratios in Table 3 to the average of the experimental data in *Ramdani et al.* [1987] and *Schmidbauer and Keller* [2006], where the oxidation parameter *z* varies from 0 to 1, representing a transformation from Fe<sub>3</sub>O<sub>4</sub> (*z* = 0) to  $\gamma$ -Fe<sub>2</sub>O<sub>3</sub> (*z* = 1) [*Readman and O'Reilly*, 1972; *Ge et al.*, 2014]. The relationship between the oxidation parameter *z* and the lattice parameter *a* is shown in Figure 7b, where *z* is shown to increase with the decreasing size of the cubic unit cell.

**Table 2.** Atomic Composition Calculated From Each Cumulative EEL Spectra Displayed as a Molar Ratio

Spectrum	Element			
	O		Fe	
	Atomic Ratio (O)	Content (at %)	Atomic Ratio (O)	Content (at %)
A	1.00 ± 0.00	55	0.82 ± 0.05	45
B	1.00 ± 0.00	55	0.82 ± 0.05	45
C	1.00 ± 0.00	57	0.75 ± 0.05	43

The relationship between the oxidation parameter *z* and the lattice parameter *a* is shown in Figure 7b, where *z* is shown to increase with the decreasing size of the cubic unit cell.

Figure 8 provides information on the effect of reaction temperature on the magnetic hysteresis of the

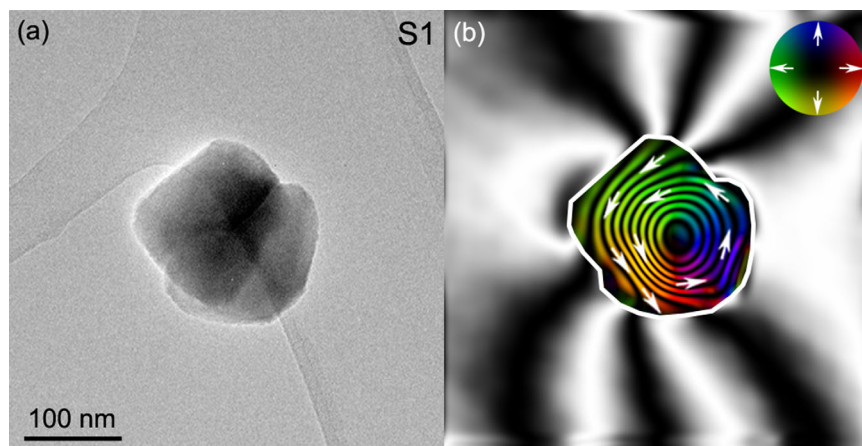


**Figure 4.** (a) BF TEM image of an individual native Fe<sub>3</sub>O<sub>4</sub> particle (~180 nm in diameter, Sample S1); and (b) a magnetic induction map of the particle shown in Figure 4a. The magnetic contour spacing is 0.26 radians and magnetization direction is depicted in the color wheel.

reaction products and FORC diagrams of Samples S1 and S220. The coercivity ( $B_c$ ) distribution in each sample is shown by horizontal profiles along the  $B_u = 0$  axis of FORC data measured from Samples S1–S220 (Figure 8a). In addition, the measured values for coercivity of remanence ( $B_{cr}$ ) and  $B_c$  are summarized in Table 4. A general trend of increasing  $B_{cr}$  values and  $B_c$  profiles with reaction temperature and oxidation can be seen up to 180°C, and exhibits a marked decrease thereafter, which is in agreement with the study of Ge *et al.* [2014]. The ratios of  $M_{rs}/M_s$  versus  $H_{cr}/H_c$  are plotted in Figure 8b (a “Day plot” [Day *et al.*, 1977]) for the different reaction products. All the samples lie within the PSD region [Dunlop, 2002], however, Sample S220 plots distinctly toward the SD region, in agreement with the previous studies [Liu *et al.*, 2004]. The FORC diagram of Sample S1 (Figure 8c) displayed PSD/SD type behavior with a distinct peak centered at a  $B_c$  value of ~22 mT [Muxworthy and Dunlop, 2002]. The peak in the FORC diagram of Sample S220 (Figure 8d) depicts similar behavior, but is centered at a lower  $B_c$  value of ~18 mT.

Curie temperatures ( $T_C$ ) were determined using the second-derivative method [Tauxe, 1998] and the relationship with oxidation parameter  $z$  is presented in Figure 9a. Values of  $T_C$  were calculated as  $583 \pm 5^\circ\text{C}$  for Samples S1 and S120, which is marginally above that of stoichiometric Fe<sub>3</sub>O<sub>4</sub> [Dunlop and Özdemir, 2001]. The  $T_C$  of Samples S140 and S160 was slightly higher and a linear increase of  $T_C$  with temperature can be seen in Samples S180–S220, with a maximum  $T_C$  of  $649 \pm 5^\circ\text{C}$ , which is in good agreement with that of  $\gamma$ -Fe<sub>2</sub>O<sub>3</sub> [Dunlop and Özdemir, 2001]. This trend of increasing  $T_C$  with reaction temperature is similar to that seen in the oxidation process of titanomagnetites [Readman and O’Reilly, 1972]. The thermomagnetic curve of Sample S220 is presented in Figure 9b and the large difference between the heating and cooling curves

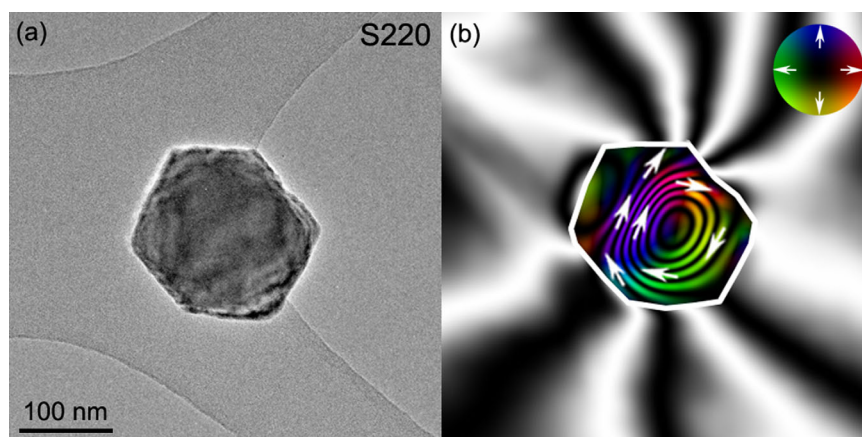


**Figure 5.** (a) BF TEM image of an individual  $\gamma$ -Fe<sub>2</sub>O<sub>3</sub> particle (~200 nm in diameter, Sample S220); and (b) a magnetic induction map of the particle shown in Figure 5a. The magnetic contour spacing is 0.26 radians and magnetization direction is depicted in the color wheel.

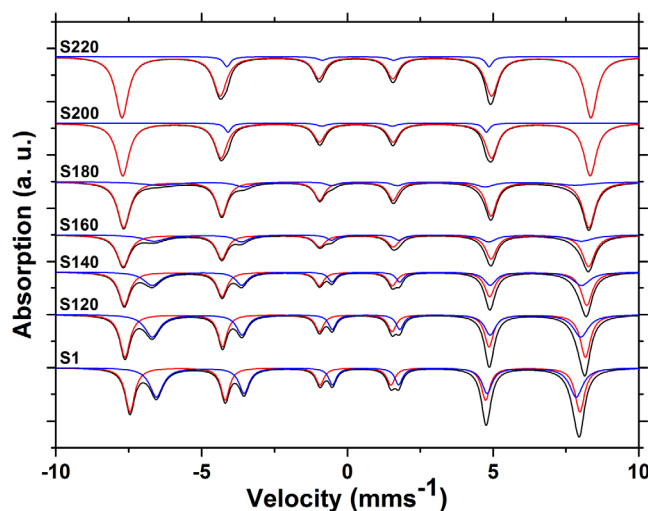


**Figure 6.** Mössbauer spectra of Samples S1–S220 (black) follow the maghemization of  $\text{Fe}_3\text{O}_4$  as a function of reaction temperature. Mössbauer parameters were determined by fitting two sextets,  $St_1$  (red) and  $St_2$  (blue).

particles to be  $\sim 150$  to  $\sim 250$  nm in diameter and off-axis electron holography revealed their PSD nature. However, Mössbauer analysis of Sample S1 exhibited sextets with hyperfine parameters more indicative of nonstoichiometric  $\text{Fe}_3\text{O}_4$ , with an approximate composition of 59% magnetite and 41% maghemite. Increasing the reaction temperature led to the development of additional peaks in the XRD patterns of Samples S120–S200, and Sample S220 displayed an XRD pattern characteristic of  $\gamma\text{-Fe}_2\text{O}_3$ . This structural phase transformation is reinforced by the SAED pattern of Sample S220 and development of small peaks in the EEL spectra of Fe  $L_{2,3}$  edge further confirm the oxidation to  $\gamma\text{-Fe}_2\text{O}_3$ . TEM imaging shows the reaction products heated to 220°C retained their shape and without a marked change during the transition to  $\gamma\text{-Fe}_2\text{O}_3$ . Mössbauer spectra of Samples S120–S200 demonstrate a reduction in magnetite content and conversion to maghemite with increasing reaction temperature, where Sample S220 displays a typical spectrum of  $\gamma\text{-Fe}_2\text{O}_3$  [Da Costa et al., 1995; Schmidbauer and Keller, 2006].

#### 4.2. Oxidation Mechanism

Oxidation of inverse spinel structured  $\text{Fe}_3\text{O}_4$  under low-temperature conditions is known to involve topotactic transformation where the original morphology is maintained throughout [Gallagher et al., 1968; Cornell and Schwertmann, 2003]. The reaction proceeds by outward migration of  $\text{Fe}^{2+}$  cations toward the surface of the crystal, thereby creating cation vacancies, and absorbed oxygen atoms at the surface oxidize the migrating cations to form a shell of  $\gamma\text{-Fe}_2\text{O}_3$ . In terms of diffusion pathways, when  $\alpha\text{-Fe}_2\text{O}_3$  is reduced to  $\text{Fe}_3\text{O}_4$ , the newly formed  $\text{Fe}_3\text{O}_4$  {111} planes are parallel to the original  $\alpha\text{-Fe}_2\text{O}_3$  {006} planes, with the latter considered favorable planes for oxygen diffusion during thermal reduction [Almeida et al., 2012]. Hence, in the reverse process of oxidation, the  $\text{Fe}^{2+}$  cations are suggested to preferentially diffuse along the  $\text{Fe}_3\text{O}_4$  {111} planes,

is indicative of possible inversion to hematite, which can be expected with heating of  $\gamma\text{-Fe}_2\text{O}_3$  to elevated temperatures [Özdemir and Dunlop, 1988].

## 4. Discussion

### 4.1. Overview

This study has followed the maghemization of  $\text{Fe}_3\text{O}_4$  grains in the PSD size range as a function of reaction temperature and the associated effect on their magnetic properties. The XRD pattern of Sample S1 is in good agreement of pure  $\text{Fe}_3\text{O}_4$ , which is reinforced by complementary SAED and characteristic O 1s K/Fe 2p  $L_{2,3}$  edges in the associated EEL spectra. Further, TEM imaging showed the

**Table 3.** Mossbauer Parameters of Sextets  $St_1$  and  $St_2$  of Figure 6 Determined for Samples S1–S220<sup>a</sup>

Sample	$B_{\text{hf}}$ (T)		$IS$ ( $\text{mm s}^{-1}$ )		$QS$ ( $\text{mm s}^{-1}$ )		$W$ ( $\text{mm s}^{-1}$ )		$\delta_{\text{aver}}$	Magnetite (wt %)	$F_B/F_A$	$z$
	$St_1$	$St_2$	$St_1$	$St_2$	$St_1$	$St_2$	$St_1$	$St_2$				
S1	47.9	44.7	0.28	0.65	−0.01	0.01	0.39	0.55	0.46	59	0.93	0.33
S120	49.0	45.6	0.29	0.66	−0.01	0.01	0.42	0.63	0.46	56	0.79	0.53
S140	49.3	45.7	0.30	0.67	−0.01	0.02	0.46	0.71	0.44	50	0.63	0.53
S160	49.6	45.5	0.32	0.67	−0.01	0.05	0.52	0.99	0.41	37	0.38	0.71
S180	49.5	44.3	0.32	0.65	0.00	0.04	0.51	1.62	0.39	25	0.23	0.85
S200	49.8	47.5	0.32	0.41	0.00	0.06	0.51		0.33	−0.55	0.13	0.96
S220	49.9	48.2	0.32	0.43	0.01	0.06	0.53		0.33	−1.9		0.99

<sup>a</sup> $B_{\text{hf}}$  = magnetic hyperfine field,  $IS$  = isomer shift with regard to metallic Fe;  $QS$  = quadrupole splitting and  $W$  = line width of the outermost lines of a sextet (FWHM).  $\delta_{\text{aver}}$  = weighted average isomer shift of sextets  $St_1$  and  $St_2$ . Magnetite (wt %) calculated using the model of Da Costa et al. [2014].  $F_B/F_A$  = relative area ratio of sextet B to sextet A.  $F_B/F_A$  is calculated assuming  $[\text{Fe}_B^{2+}]$   $[\text{Fe}_A^{3+}\text{Fe}_B^{3+}]$ . The estimate for  $z$  was made by comparing  $F_B/F_A$  ratios to those in the literature [Ramdani et al., 1987; Schmidbauer and Keller, 2006].

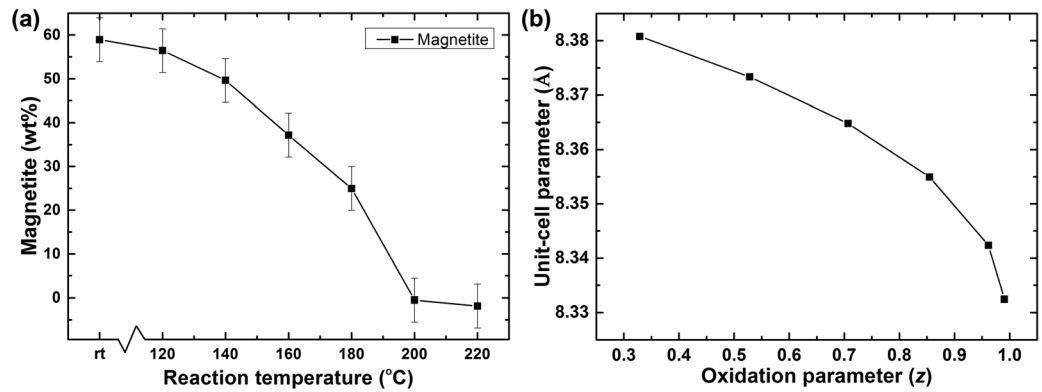


**Figure 7.** (a) Magnetite content in Samples S1–S220 as a function of increasing reaction temperature. (b) Relationship between the oxidation parameter  $z$  and the unit cell lattice parameter  $a$ .

with their relatively large lattice plane spacing of 4.79 Å providing a low energy diffusion pathway. For example, the HAADF image in Figure 3b shows the {111} planes to lie normal to the surface edge in the Fe<sub>3</sub>O<sub>4</sub> grain and would provide an easy route for cation diffusion to the surface for oxidation. The fully oxidized inverse spinel structure of  $\gamma$ -Fe<sub>2</sub>O<sub>3</sub> can be written as Fe<sup>3+</sup> [Fe<sup>3+</sup><sub>5/3</sub> □<sub>1/3</sub>] O<sub>4</sub><sup>2-</sup>, where the octahedral sites are enclosed by the brackets and □ denotes a lattice vacancy. The composition calculated quantitatively from the EEL spectra shows the surface of the Fe<sub>3</sub>O<sub>4</sub> grain in Sample S140 (Spectrum C, Figure 3) to exhibit a slightly higher O content than toward its center. By implication, the observed lower surface Fe content provides evidence for the surface oxidation mechanism with the formation of core-shell Fe<sub>3</sub>O<sub>4</sub>/ $\gamma$ -Fe<sub>2</sub>O<sub>3</sub> structures with increasing reaction temperature. However, the change in stoichiometry during oxidation of significantly larger Fe<sub>3</sub>O<sub>4</sub> grains is considered to proceed more uniformly.

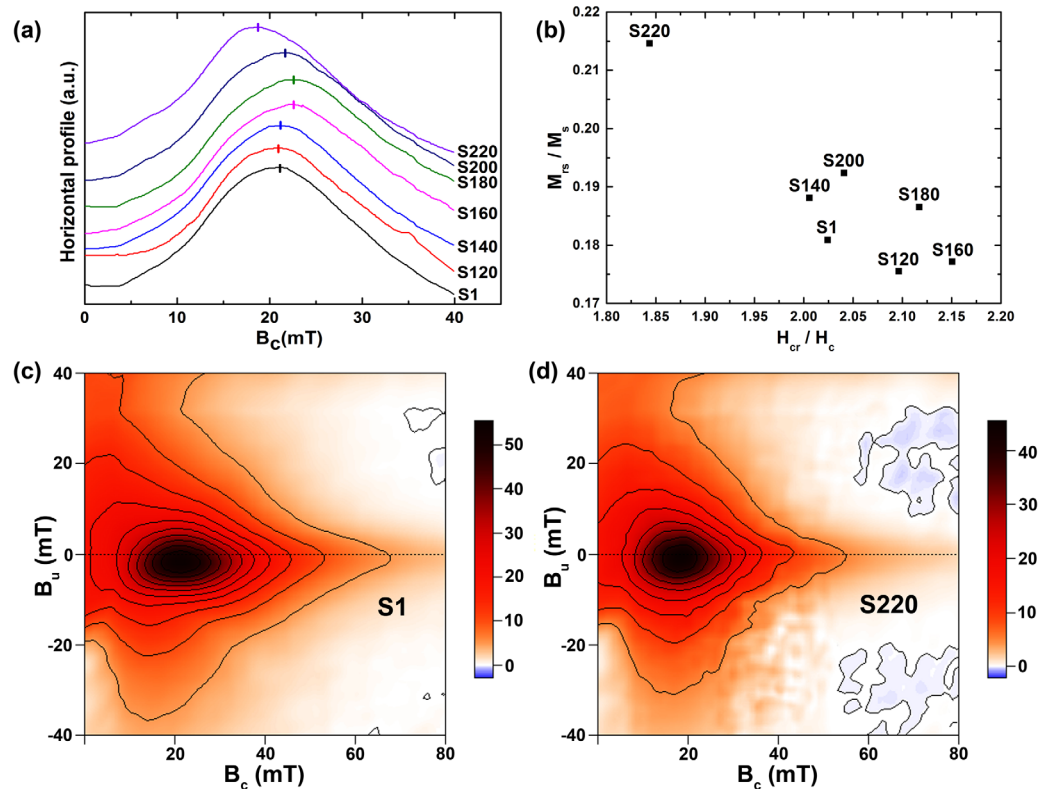


**Figure 8.** Magnetic properties of Samples S1–S220 as a function of increasing reaction temperature. (a) Graph of  $B_c$  profiles along the  $B_u = 0$  axis extracted from the FORC diagrams, with the maximum value of the profile marked; and (b) a Day plot of the reaction products. (c, d) Normalized FORC diagrams of Samples (c) S1 and (d) S220, acquired at room temperature.

**Table 4.** Summary of Room-Temperature Hysteresis Parameters and Curie Temperatures of Samples S1–S220

Sample	$B_c$ (mT)	$B_{cr}$ (mT)	$B_{cr}/B_c$	$M_s$	$M_{rs}/M_s$	$T_c$ (°C)
S1	12.37	25.04	2.02	0.47	0.18	583
S120	12.05	25.26	2.10	0.34	0.18	583
S140	12.35	24.77	2.01	0.26	0.19	589
S160	12.96	27.87	2.15	0.25	0.18	589
S180	13.33	28.22	2.12	0.14	0.19	608
S200	12.51	25.53	2.04	0.34	0.19	629
S220	12.21	22.51	1.84	0.23	0.21	649

### 4.3. Effect of Oxidation on Magnetic Properties

In  $Fe_3O_4$ ,  $Fe^{2+}$  cations occupies the octahedral B-sites, whilst  $Fe^{3+}$  ions occupies both tetrahedral A and octahedral B-sites, and hence, the magnetic moments of the  $Fe^{3+}$  ions are mutually compensated and the net moment is attributed to the  $Fe^{2+}$  cations [Mathew and Juang, 2007]. In contrast, the ferrimagnetism of  $\gamma$ - $Fe_2O_3$  is the result of an average excess per formula weight  $Fe_{8/3}O_4$  of  $2/3$  of an  $Fe^{3+}$  ion on the B sublattice [Dunlop and Özdemir, 2001]. The  $T_c$  values for Samples S1 and S220 were indicative of  $Fe_3O_4$  and  $\gamma$ - $Fe_2O_3$ , respectively, whilst their FORC diagrams display PSD/SD type behavior with distinct peaks centered at  $\sim 22$  and  $\sim 18$  mT, respectively. Construction of magnetic induction maps from the off-axis electron holograms complemented the FORC data by visualizing the PSD domain state nature of both the  $Fe_3O_4$  and  $\gamma$ - $Fe_2O_3$  grains. Interestingly, during the oxidation process from  $Fe_3O_4$  to  $\gamma$ - $Fe_2O_3$ , the  $B_c$  and  $B_{cr}$  values generally increased with reaction temperature up to  $180^\circ C$ , with subsequent decrease thereafter. Ge *et al.* [2014] reported a similar trend during oxidation of  $Fe_3O_4$  particles in the PSD size range, which they interpreted using a micromagnetic numerical model: for PSD grains near the critical SD grain size boundary, as the  $Fe^{2+}$  cations diffuse toward the surface of the particle and the  $\gamma$ - $Fe_2O_3$  shell thickness increases through oxidation, the diameter of the  $Fe_3O_4$  core decreases as a consequence. As the  $Fe_3O_4$  core becomes smaller, the overall magnetic strength of the grain decreases due to the lower  $M_s$  of the  $\gamma$ - $Fe_2O_3$  skin, whilst exchange coupling of the  $Fe_3O_4$  core to the  $\gamma$ - $Fe_2O_3$  skin maintains the high magnetocrystalline anisotropy, and at a point, the minimum energy domain structure is more SD-like. As oxidation proceeds the small  $Fe_3O_4$  core shrinks sufficiently so that it is unable to provide a significant influence on the  $B_{cr}$ , which collapses markedly as the grain reverts to a vortex structure. For larger PSD grains, the grains remain in a vortex state throughout the oxidation process, but vorticity of the magnetic domain state reduces as the  $\gamma$ - $Fe_2O_3$  skin grows. The magnetically harder and slightly more uniform domain structures result in a trend of increasing  $B_c$  until the  $Fe_3O_4$  core almost disappears when both parameters decrease significantly, which is consistent with the experimental data and supports the proposed mechanism of maghemization proceeding through the formation of core-shell  $Fe_3O_4/\gamma$ - $Fe_2O_3$  structures. Due to the rather subtle changes observed in the  $B_c$  values and FORC diagrams, the transition from vortex state to vortex with reduced vorticity is considered to be the dominant mechanism in this study. It appears unlikely given the small increases

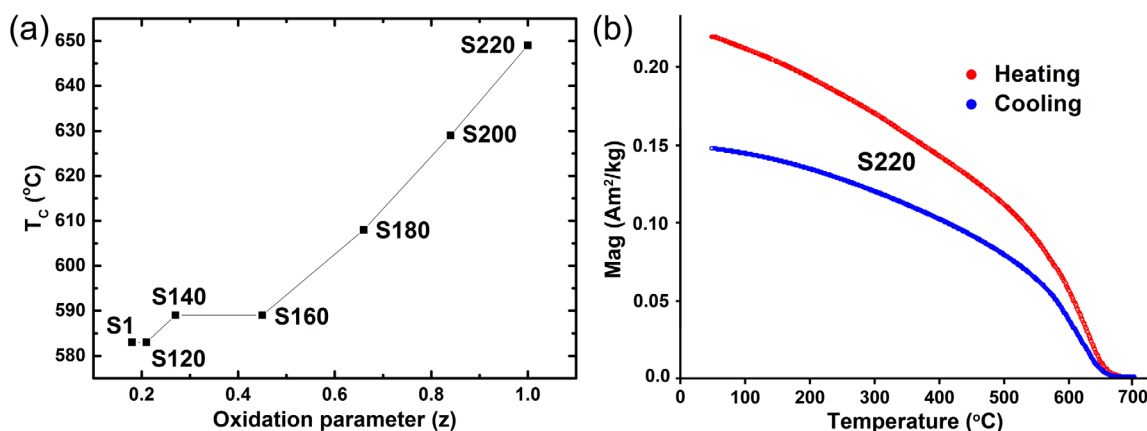


**Figure 9.** (a) Curie temperatures of Samples S1–S220 as a function of oxidation parameter  $z$ . (b) Thermomagnetic curve of Sample S220. Heating was performed in flowing helium in a field of 300 mT.

in coercivity that magnetoelastic effects due to induced stress contribute significantly to the resulting magnetic properties.

#### 4.4. Implications for Paleomagnetic Studies

From the above observations, the reliability of the magnetic remanence of maghemitized rocks is called into question; the process of oxidation will lead to the acquisition of a new chemical remanent magnetization (CRM). Due to the shell growth mechanism, the original  $\text{Fe}_3\text{O}_4$  phase in the core will effect the magnetic alignment of the  $\gamma\text{-Fe}_2\text{O}_3$  shell [Ge *et al.*, 2014]. It is likely that on average for a distribution of the particles the original magnetization direction will be retained. However, obtaining an paleointensity estimate may not be accurate for two reasons: (1) the core/shell CRM acquisition model may not always couple and the CRM of individual particles may not be aligned with the original remanence and (2) whilst it might be theoretically possible to recover the paleointensity information from a  $\gamma\text{-Fe}_2\text{O}_3$  sample,  $\gamma\text{-Fe}_2\text{O}_3$  is generally unstable to heating, as evidenced by the thermomagnetic curve of Sample S220, and samples dominated by this phase are, therefore, likely to fail Thellier-type or other heating paleointensity protocols. It is also recognized that potential differences exist between these experimental results, which involve oxygen addition, compared to that undergone in mid-ocean ridges that may favor a Fe-removal mechanism for oxidation.

## 5. Conclusions

This study has investigated the maghemization of  $\text{Fe}_3\text{O}_4$  grains in the PSD size range and the effect of this oxidation process on their magnetic properties. Complementary methods of XRD and Mossbauer spectroscopy followed this phase transformation as a function of temperature and showed the onset of oxidation was most pronounced at 160°C, with a reaction temperature of 220°C producing pure  $\gamma\text{-Fe}_2\text{O}_3$ . The phase transformation is confirmed by EELS analysis of the O 1s K/Fe 2p  $L_{2,3}$  edges acquired from the precursor  $\text{Fe}_3\text{O}_4$  grains and fully oxidized  $\gamma\text{-Fe}_2\text{O}_3$  grains. High-resolution HAADF imaging and localized EELS analysis revealed evidence to suggest the surface to be more oxidized, supporting the formation of a core-shell  $\text{Fe}_3\text{O}_4/\gamma\text{-Fe}_2\text{O}_3$  structure. Off-axis electron holography allowed for construction of magnetic induction maps of individual  $\text{Fe}_3\text{O}_4$  and  $\gamma\text{-Fe}_2\text{O}_3$  grains, revealing their PSD (vortex) nature in both cases, which is supported by corresponding first-order reversal curves characteristic of PSD states. Thermomagnetic curves showed an increase of  $T_C$  with reaction temperature that is consistent with maghemization process. The coercivity of the magnetite grains was shown to increase with reaction temperature up to 180°C, but decrease thereafter. This magnetic behavior is attributed to exchange coupling between a  $\gamma\text{-Fe}_2\text{O}_3$  shell with the  $\text{Fe}_3\text{O}_4$  core resulting in an energy minimum of SD state or a vortex state with reduced vorticity, with the latter considered the dominant mechanism in this study. Once fully oxidized to  $\gamma\text{-Fe}_2\text{O}_3$ , the domain states revert back to vortices with slightly reduced coercivity. It is suggested that heavily maghemized samples may not retain meaningful paleomagnetic signals.

#### Acknowledgments

The authors would like to thank the Natural Environment Research Council for funding (NERC grant NE/H00534X/1). Thanks also go to the Center for Electron Nanoscopy at the Technical University of Denmark for use of their microscopy facilities. The data for this paper are available at NERC-designated data center for the Earth sciences, the National Geoscience Data Centre.

#### References

- Almeida, T. P., M. W. Fay, Y. Zhu, T. W. Hansen, R. E. Dunin-Borkowski, and P. D. Brown (2012), Environmental TEM investigation of the reduction of  $\alpha\text{-Fe}_2\text{O}_3$  nanorods under  $\text{H}_2$  atmosphere, *J. Phys. Conf. Ser.*, *371*, 012049.
- Almeida, T. P., T. Kasama, A. R. Muxworthy, W. Williams, L. Nagy, P. D. Brown, and R. E. Dunin-Borkowski (2014), Visualised effect of oxidation on magnetic recording fidelity in pseudo-single-domain magnetite particles, *Nat. Commun.*, *5*, 5154, doi:10.1038/ncomms6154.
- Bleil, U., and N. Petersen (1983), Variation in magnetization intensity and low-temperature titanomagnetite oxidation of ocean floor basalts, *Nature*, *301*, 384–388.
- Chen, J., D. J. Huang, A. Tanaka, C. F. Chang, S. C. Chung, W. B. Wu, and C. T. Chen (2004), Magnetic circular dichroism in Fe 2p resonant photoemission of magnetite, *Phys. Rev. B*, *69*, 085107.
- Chen, S.-Y., A. Gloter, A. Zobelli, L. Wang, C.-H. Chen, and C. Colliex (2009), Electron energy loss spectroscopy and *ab initio* investigation of iron oxide nanomaterials grown by a hydrothermal process, *Phys. Rev. B*, *79*, 104,103.
- Colliex, C., T. Manoubi, and C. Ortiz (1991), Electron-energy-loss-spectroscopy near-edge fine structures in the iron-oxygen system, *Phys. Rev. B*, *44*, 11,402–11,411.
- Cornell, R. M., and U. Schwertmann (2003), *The Iron Oxides, Structure, Properties, Reactions, Occurrence and Uses*, pp. 664, John Wiley, Weinheim, Germany.
- Crocombette, J. P., M. Pollak, F. Joliet, N. Thromat, and M. Gautier-Soyer (1995), X-ray-absorption spectroscopy at the Fe  $L_{2,3}$  threshold in iron oxides, *Phys. Rev. B*, *52*, 3143–3150.
- Cullity, B. D., and S. R. Stock (2001), *Elements of X-ray Diffraction*, 3rd ed., Prentice Hall, N. J.
- Da Costa, G. M., E. De Grave, P. M. A. De Bakker, and R. E. Vandenberghe (1995), Influence of nonstoichiometry and the presence of maghemite on the Mössbauer spectrum of magnetite, *Clays Clay Miner.*, *43*, 656–668.
- Da Costa, G. M., C. Blanco-Andujar, E. De Grave, and Q. A. Pankhurst (2014), Magnetic nanoparticles for in vivo use: A critical assessment of their composition, *J. Phys. Chem. B*, *118*, 11,738–11,746.

- Day, R., M. Fuller, and V. A. Schmidt (1977), Hysteresis properties of titanomagnetites: Grain size and composition dependence, *Phys. Earth Planet. Inter.*, *13*, 260–267.
- Dunin-Borkowski, R. E., M. R. McCartney, and D. J. Smith (1998), Off-axis electron holography of magnetic materials, *Rec. Res. Dev. Appl. Phys.*, *1*, 119–131.
- Dunlop, D. J. (2002), Theory and application of the Day plot ( $M_r/M_s$  versus  $H_{cr}/H_c$ ), 1. Theoretical curves and tests using titanomagnetite data, *J. Geophys. Res.*, *107*(B3), 2056, doi:10.1029/2001JB000486.
- Dunlop, D. J., and Ö. Özdemir (2001), *Rock Magnetism: Fundamentals and Frontiers*, pp. 577, Cambridge Univ. Press, N. Y.
- Fujii, T., F. M. F. De Groot, G. A. Sawatzky, F. C. Voogt, T. Hibma, and K. Okada (1999), In situ XPS analysis of various iron oxide films grown by NO<sub>2</sub>-assisted molecular-beam epitaxy, *Phys. Rev. B*, *59*, 3195–3202.
- Gallagher, K. J., W. Feitknecht, and U. Mannweiler (1968), Mechanism of oxidation of magnetite to  $\gamma$ -Fe<sub>2</sub>O<sub>3</sub>, *Nature*, *217*, 1118–1121.
- Ge, K., W. Williams, Q. Liu, and Y. Yu (2014), Effects of the core-shell structure on the magnetic properties of partially oxidized magnetite grains: Experimental and micromagnetic investigations, *Geochem. Geophys. Geosyst.*, *15*, 2021–2038, doi:10.1002/2014GC005265.
- Gloter, A., A. Douiri, M. Tence, and C. Colliex (2003), Improving energy resolution of EELS spectra: An alternative to the monochromator solution, *Ultramicroscopy*, *96*, 385.
- Kasama, T., R. E. Dunin-Borkowski, and M. Beleggia (2011), Electron holography of magnetic materials, in *Holography—Different Fields of Application*, edited by F. A. M. Ramirez, pp. 53–80, InTech, Rijeka.
- Krásá, D., V. P. Shcherbakov, T. Kunzmann, and N. Petersen (2005), Self-reversal of remanent magnetization in basalts due to partially oxidized titanomagnetites, *Geophys. J. Int.*, *162*, 115–136.
- Liu, Q. S., S. K. Banerjee, M. J. Jackson, C. L. Deng, Y. X. Pan, and R. X. Zhu (2004), New insights into partial oxidation model of magnetites and thermal alteration of magnetic mineralogy of the Chinese loess in air, *Geophys. J. Int.*, *158*, 506–514, doi:10.1111/j.1365-246X.2004.02348.x.
- Mathew, D. S., and R.-S. Juang (2007), An overview of the structure and magnetism of spinel ferrite nanoparticles and their synthesis in microemulsions, *Chem. Eng. J.*, *129*, 51–65.
- Matzka, J., D. Krásá, T. Kunzmann, A. Schult, and N. Petersen (2003), Magnetic state of 10–40 Ma old ocean basalts and its implications for natural remanent magnetization, *Earth Planet. Sci. Lett.*, *206*, 541–553, doi:10.1016/s0012-821x(02)01094-4.
- Muxworthy, A. R., and D. Dunlop (2002), First-order reversal curve (FORC) diagrams for pseudo-single-domain magnetites at high temperature, *Earth Planet. Sci. Lett.*, *203*, 369–382.
- O'Reilly, W. (1984), *Rock and Mineral Magnetism*, 220 pp., Blackie Acad. and Prof., Glasgow, U. K.
- Özdemir, Ö., and D. Dunlop (1988), Crystallization remanent magnetization during the transformation of maghemite to hematite, *J. Geophys. Res.*, *93*, 6530–6544.
- Ramdani, A., J. Steinmetz, C. Gleitzer, J. M. D. Coey, and J. M. Friedt (1987), Perturbation de L'échange électronique rapide par les lacunes cationiques dans Fe<sub>3-x</sub>O<sub>4</sub> ( $x \leq 0,09$ ), *J. Phys. Chem. Solids*, *48*, 217–228.
- Readman, P. W., and W. O'Reilly (1972), Magnetic Properties of Oxidized (Cation-Deficient) Titanomagnetites (Fe, Ti, □)<sub>3</sub>O<sub>4</sub>, *J. Geomagn. Geoelectr.*, *24*, 69–90.
- Schmidbauer, E., and M. Keller (2006), Magnetic hysteresis properties, Mossbauer spectra and structural data of spherical 250 nm particles of solid solutions Fe<sub>3</sub>O<sub>4</sub>- $\gamma$ -Fe<sub>2</sub>O<sub>3</sub>, *J. Magn. Magn. Mater.*, *297*, 107–117.
- Tauxe, L. (1998), *Paleomagnetic Principles and Practice*, Kluwer Acad., Dordrecht, Netherlands.
- van Aken, P. A., and S. Lauterbach (2003), Strong magnetic linear dichroism in Fe L<sub>23</sub> and O K electron energy-loss near-edge spectra of antiferromagnetic hematite  $\alpha$ -Fe<sub>2</sub>O<sub>3</sub>, *Phys. Chem. Miner.*, *30*, 469.
- Van Velzen, A. J., and J. D. A. Zijdeveld (1995), Effects of weathering on single-domain magnetite in Early Pliocene marine marls, *Geophys. J. Int.*, *121*, 267–278.